

FULL PAPER

Open Access



Geomagnetic paleointensity dating of mid-ocean ridge basalts from the neo-volcanic zone of the Central Indian Ridge

Yutaka Yoshimura^{1*} and Masakazu Fujii^{2,3}

Abstract

Describing the evolution of the neo-volcanic zone in the spreading ridge is essential for understanding the dynamics and environments of abyssal basins. However, the absolute dating of ocean floor basalts is generally difficult. As a characteristic age indicator, absolute intensity of past geomagnetic field (absolute paleointensity, API) is useful to date ocean floor basalts. In this study, we adopted the Tsunakawa–Shaw method to measure APIs of whole-rock seafloor basalts collected from a conical cone on the Central Indian Ridge and performed rock magnetic experiments. We conducted the experiments on a total of 18 specimens (two or three specimens from each of eight lava sites). Six specimens from two lava sites with different morphologies (pillow and sheet), three for each, passed the acceptance criteria. API means at site level are 33.0 ± 1.0 and 35.8 ± 1.7 μT , respectively. The similarity of API site means suggests that they erupted within a short period. These site-level API means are approximately 0.7 to 0.8 times the present geomagnetic intensity of 46.0 μT at the sampling sites. The accepted specimens show higher Curie temperature, lower initial intensity of natural remanent magnetization, higher ratio of saturation remanence to saturation magnetization (M_{rs}/M_s), and signal of harder magnetic mineral than rejected ones. Our primary comparison between the two site-level API means and the 1590–present high-resolution IGRF-13 + gufm1 model constrains that the eruption timing of the conical cone to be < 1590 CE. When we compared the two site-level API means with the paleointensity curves calculated from the BIGMUDI4k.1 and ArchKalmag14 k.r, we found that they overlap in the period of -7575 to -1675 CE or -25 to 1590 CE, which may be the eruption timing of the conical cone. We concluded that timing of recent volcanic eruption in abyssal environment could be investigated by using appropriate rock magnetic selection and carefully examined API.

Keywords Central Indian Ridge, Neo-volcanic zone, Mid-ocean ridge basalt, Paleointensity, Tsunakawa-Shaw method, Paleointensity dating

*Correspondence:

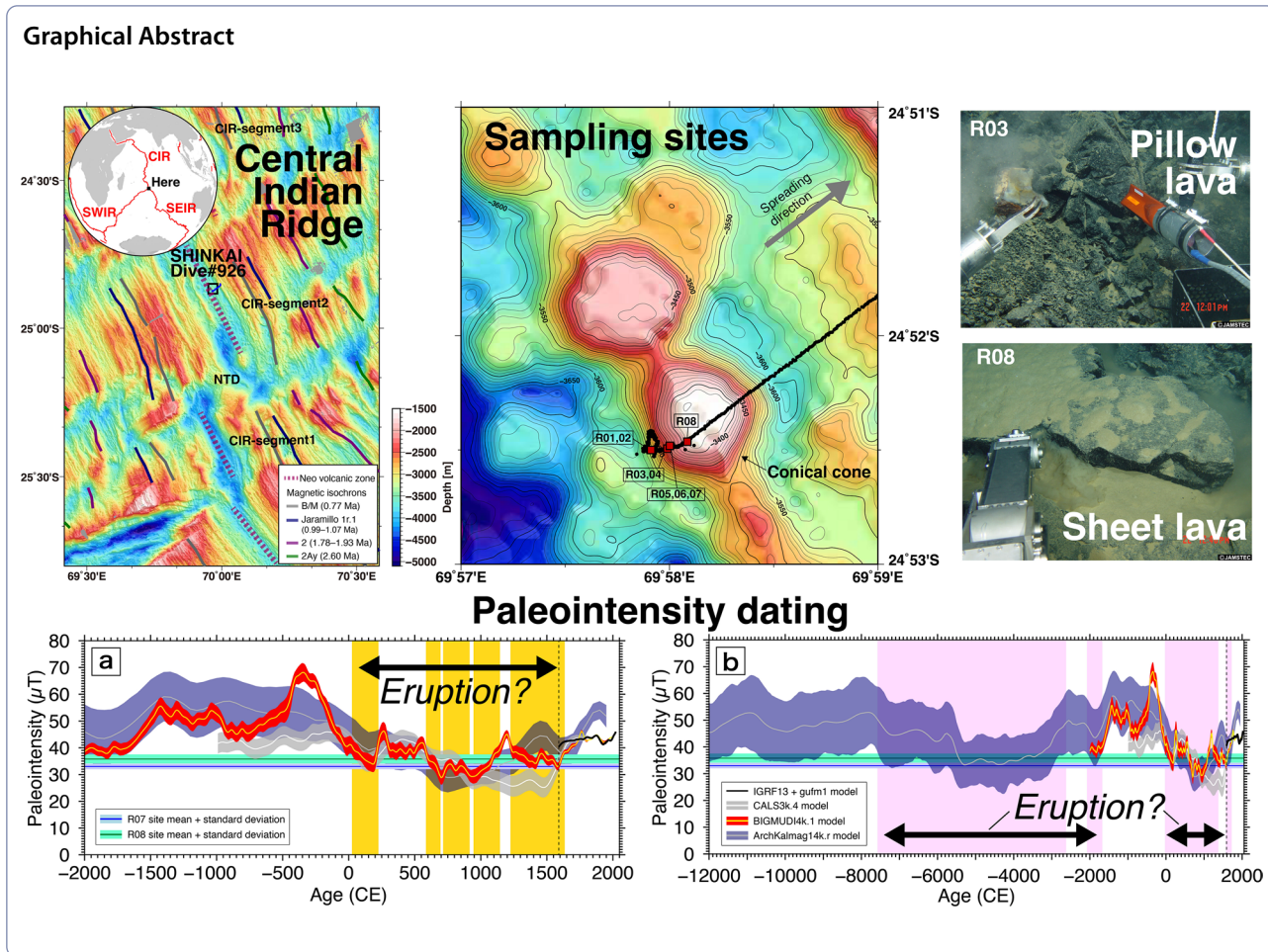
Yutaka Yoshimura

yoshimura.yutaka.36w@kyoto-u.jp

Full list of author information is available at the end of the article



© The Author(s) 2024. **Open Access** This article is licensed under a Creative Commons Attribution 4.0 International License, which permits use, sharing, adaptation, distribution and reproduction in any medium or format, as long as you give appropriate credit to the original author(s) and the source, provide a link to the Creative Commons licence, and indicate if changes were made. The images or other third party material in this article are included in the article's Creative Commons licence, unless indicated otherwise in a credit line to the material. If material is not included in the article's Creative Commons licence and your intended use is not permitted by statutory regulation or exceeds the permitted use, you will need to obtain permission directly from the copyright holder. To view a copy of this licence, visit <http://creativecommons.org/licenses/by/4.0/>.



Introduction

Volcanic activities in the mid-ocean ridges mainly occur in a focused area of the sea-floor spreading axis, known as neo-volcanic zones (NVZs). They are characterized by young volcanic features and symmetric magnetic anomalies (e.g., Macdonald et al. 1984; Smith and Cann 1990; Okino et al. 2015). The evolution of NVZs contributes to both long-term phenomena, like the formation of abyssal basins, and short-term ones, such as neotectonic activity, global material cycles, and the persistence of the deep-sea ecosystem. However, understanding of the evolution with absolute dating has not been achieved. This is because a detailed age, especially less than 10⁴ years, cannot be determined from the record of geomagnetic reversals recognized from magnetic anomalies and radiometric dating. The observation of lava superposition and/or chemical composition transition can only provide the relative age of seafloor lava. Reconstructions of variations in absolute intensity of past geomagnetic field (absolute paleointensity, API) recorded in in-situ lavas,

combined with global geomagnetic models, may provide age estimates. However, precise measurements of API using mid-ocean ridge basalts (MORBs) have not yet been established.

Because glass hosting remanent magnetization-carrying minerals in its interior is thought to protect the magnetic minerals from weathering, many previous studies used submarine basaltic glass from the quenched margins of MORBs to obtain high-quality APIs (e.g., Juarez et al. 1998; Pick and Tauxe 1993a,b; Mejia et al. 1996; Gee et al. 2000; Carlut and Kent 2000; Riisager et al. 2003; Carlut et al. 2004; Bowles et al. 2006). For example, Bowles et al. (2006) conducted API measurements for age determination using near-axis MORB glasses collected from the East Pacific Rise at 9°–10°N. They found an age difference of 150 to 200 years between the old and new lavas using a contrast in APIs.

Non-glass MORBs have also been used for API measurement; however, there are only a few studies (Dunlop and Hale 1976; Grommé et al. 1979; Prévot et al. 1983). Grommé et al. (1979) confirmed that basalts containing

titanomagnetite that had been low-temperature oxidized by seafloor weathering gave significantly low paleointensities using pillow lavas collected from the seafloor younger than 0.7 Ma. Prévot et al. (1983) showed that the linearity in the natural remanent magnetization (NRM)-thermal remanent magnetization (TRM) diagram and the partial TRM (pTRM) check test in the Thellier method could not detect the titanomagnetite alteration (change in the Curie point) during heating using MORBs collected from the FAMOUS area at 37°N of the Mid-Atlantic Ridge, which formed approximately 2000–6000 years and 10000–100000 years ago. Carlot and Kent (2002) used “zero-age” MORBs erupted in 1993 collected from the East Pacific Rise to measure APIs and identified the problem of overestimated API owing to the effects of multi-domain (MD) grains and laboratory cooling rates. In summary, when we measure APIs from non-glass MORBs, we obtain APIs that are too strong or weak because of several problems associated with magnetic minerals (alteration during heating, low-temperature oxidation, and MD grains). It is expected that there is frequently no glass left in MORBs, so it is better to be able to measure APIs even in the non-glass parts of MORBs.

The use of MORBs as targets for API measurements is valuable because it avoids the risk of overestimation by thermochemical remanent magnetizations (TCRMs). Titanomagnetite in subaerial lava often forms ilmenite lamellae by high-temperature oxidation because of relatively slow cooling (Haggerty 1991). Divided titanomagnetite into SD sizes by ilmenite lamellae is suitable for API study (Shcherbakov et al. 2019). However, Kilauea 1960 lavas in Hawaii often show overestimated API although the lavas include titanomagnetite with ilmenite lamellae (e.g., Yamamoto et al. 2003). One possible cause is TCRM acquired during the formation of ilmenite lamellae below Curie temperature (Yamamoto 2006). However, ilmenite lamellae are rare in MORBs because they are often rapidly cooled on the seafloor (Petersen et al. 1979).

Recently, the Tsunakawa–Shaw method (Yamamoto et al. 2003) has been used in various studies (e.g., Kato et al. 2018; Kitahara et al. 2018, 2021; Ahn and Yamamoto 2019; Yoshimura et al. 2020; Mochizuki et al. 2021; Biasi et al. 2021; Yamamoto et al. 2022; Pérez-Rodríguez et al. 2022). This is the latest version of the Shaw method and has following functions; anhysteretic remanent magnetization (ARM) correction, double heating technique, and low-temperature demagnetization. The ARM correction can correct laboratory heating alteration or magnetic anisotropy by using ARM acquired before and after heating. The low-temperature demagnetization can demagnetize MD grains' magnetization. The

method would work for the non-glass part of MORBs including MD grains of titanium-poor titanomagnetites. In this study, we applied the Tsunakawa–Shaw method to whole-rock MORBs from a volcanic conical cone on the Central Indian Ridge (CIR) to measure the APIs and estimate the eruption age by comparing the APIs with geomagnetic field models.

Geological setting and sampling

The CIR near the Rodriguez ridge-ridge-ridge triple junction is classified as a slow to intermediate rate spreading system, with full spreading rates of 35.5 mm/year at 10°S and 47 mm/year at 25°S (the Mid-Ocean Ridge VELOCITY, MORVEL; DeMets et al. 2010). In this study, we use the prefix CIR-SX following Briaies's (1995) ridge segment classification. The ridge axis of the CIR segment 1 (CIR-S1) to segment 4 (CIR-S4) has an axial valley of less than 10 km in width. The CIR is divided into segments by fracture zones and non-transform discontinuities (NTDs) (Parson et al. 1993; Briaies 1995). Almost at the center of the axial valley, the neo-volcanic zone, which is interpreted as the area of the most recent volcanic activity, consists of a small ridge (several hundred meters in relative height, 1–5 km wide, and more than 10 km long) parallel to the axial valley. The ridge is a series of small hills mainly composed of pillow lavas. Previous sea-surface magnetic anomaly surveys have identified the Brunhes-Matuyama boundary along the off-ridge of CIR-S1 and CIR-S2 (Honsho et al. 1996; Sato et al. 2009; Okino et al. 2015). The axial valley in CIR-S2 seems asymmetric, which suggests the NVZ recently jumped eastwards (Okino et al. 2015). Several hydrothermal fields in the NTDs between CIR-S1 and CIR-S2 also contribute to the magnetic anomalies (Fujii et al. 2016; Fujii and Okino 2018).

In this study, we used basalts from a volcanic conical cone in the NVZ of CIR-S2 (Fig. 1). The basalts were collected using the manned submersible *Shinkai 6500* during the R/V *Yokosuka* cruise of YK05-16 in 2006 and were archived at the Japan Agency for Marine-Earth Science and Technology (JAMSTEC). Rock sampling by *Shinkai 6500* was conducted along a survey line from the conical cone of the current ridge axis to the eastern rift-valley wall of CIR-S2 during the 6K#926 dive. This site is located within the eastern portion of the axial valley in the middle of the segment. A sheet lava flow was observed at the top of the conical cone. The basalts are all fresh, gray basalts with inconspicuous phenocrysts, many of which have glass rims (Additional file 1: Fig. S1). The basalts of sites 6K#926R01 and 6K#926R02 were collected from scree fields that appear to be fragments of pillow lava at the base of the conical cone.

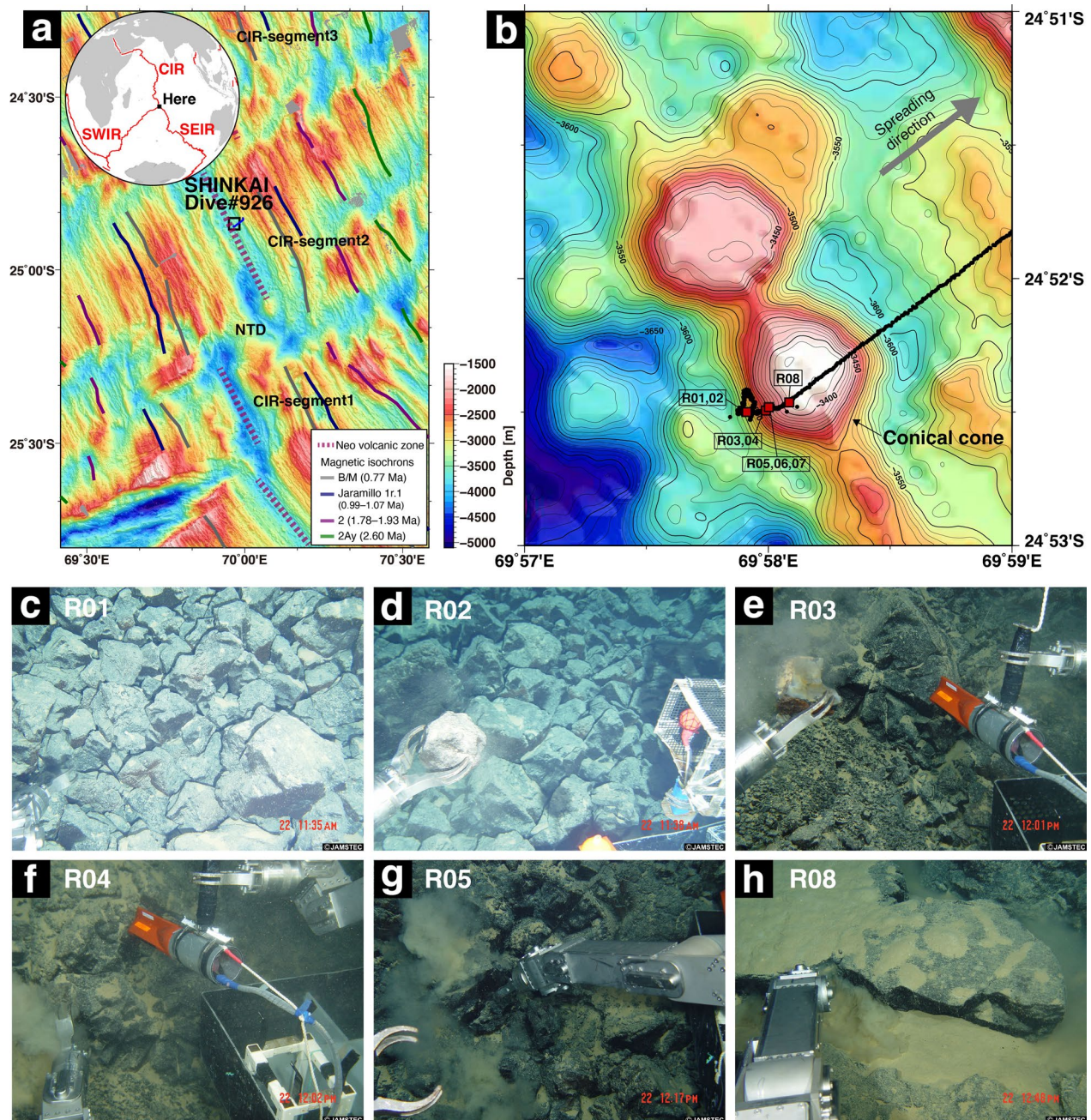


Fig. 1 Sampling locations of the neo-volcanic zone with submersible dive sites on (a) regional and (b) local bathymetric maps. Photographs of (c, d) Sites 6K#926R01 and 6K#926R02, scree field, (e, f) Sites 6K#926R03 and 6K#926R04, fresh pillow lava, (g) Site 6K#926R05 (also 6K#926R06 and 6K#926R07), broken pillow lava, (h) sheet lava near the peak of the conical cone. B/M: Brunhes-Matuyama boundary; 1r.1, 2, 2Ay: magnetic isochron of C1r.1n, C2n, C2An.1n, respectively

The basalts of sites 6K#926R03 through 6K#926R07 were collected from pillow lavas. The basalts of sites 6K#926R05 through 6K#926R07 were pillow lava with broken surfaces and exposed cross-sections. The basalt of site 6K#926R08 was collected from a sheet lava at the top of the conical cone.

Method

Grain densities, magnetic susceptibility, and NRM measurements

Four cubic specimens were cut from each of the eight lava block samples collected from the eight sites. Bulk grain densities were measured for each sites using one or two

out of the four specimens at the Atmosphere and Ocean Research Institute (AORI) of the University of Tokyo using a high-precision microbalance with a resolution of 0.01 mg and a gas pycnometer (AccuPyc 1330 Pycnometer). Magnetic susceptibility was then measured for all specimens using a ZH Instruments SM 150 L susceptibility magnetometer at AORI. The initial NRM intensity was also measured for all the specimens using an automatic spinner magnetometer with an alternating field (AF) demagnetizer (DSPIN, Natsuhara Giken) installed at AORI.

Rock magnetism

We cut chip samples for rock-magnetic measurement from 16 out of 18 specimens showing relatively strong initial NRM intensity, before API measurements (Additional file 1: Fig. S2). We conducted thermomagnetic analyses for 16 fragments of the 16 chip samples using a magnetic balance at Kyushu University (Natsuhara Giken MNB-2000M1). The chip samples were heated to 700 °C in a vacuum (<5 Pa) and a magnetic field of 100–500 mT. We also conducted magnetic hysteresis measurements on 15 fragments of the 16 chip samples and first-order reversal curve (FORC) measurements on 5 fragments of the 16 chip samples using an alternating gradient magnetometer (PMC MicroMag 2900) at the National Institute of Polar Research. Hysteresis loops were measured in the coercivity range of –0.5 to 0.5 T. In FORC measurements, B_c was from 0 to 150 mT (except for 6K#926R08, 0 to 400 mT), B_u was –60 to 60 mT. The maximum applied magnetic field was 1.0 T and the averaging time at each measurement point was 100 ms. FORCinel software (Harrison and Feinberg 2008, version 3.06) was used for analysis, and the VARIFORC algorithm of Egli (2013) was used for smoothing ($Sc0=4$, $Sb0=3$, $Sc1=Sb1=7$). The regions with low coercivity and those around $B_u=0$ were smoothed out small, whereas the other regions were smoothed out large.

Paleointensity measurements

For the API measurement experiments, we used two or three specimens from each of eight sites, 18 specimens in total. We conducted API experiments on the specimens in 7 cc non-magnetic plastic cubes and applied the Tsunakawa–Shaw method (Yamamoto et al. 2003). This is an advanced version of the Shaw method (Shaw 1974) with the addition of an ARM correction (Rolph and Shaw 1985), a double-heating technique (Tsunakawa and Shaw 1994), and low-temperature demagnetization (Ozima et al. 1964; Mochizuki et al. 2004; Smirnov et al. 2017), which can demagnetize the MD component of low-Ti titanomagnetite. The Shaw-type method uses coercivity spectra obtained from alternating field (AF) demagnetization to minimize the frequency of heating.

We used the DSPIN at Kyushu University to measure the NRM, TRM, and ARM with stepwise AF demagnetization for the Tsunakawa–Shaw method. For low-temperature demagnetization, the specimens were first soaked in liquid nitrogen in a non-magnetic dewar for 10 min, then left for 30 min at room temperature while being air-dried in a nearly zero magnetic field shield. Sixteen specimens were subjected to stepwise AF demagnetization at 2–10 mT intervals with AF steps of up to 180 mT (~40 steps in total). For TRM acquisition, specimens were heated to 610 °C in vacuum (<~10 Pa) and cooled in a DC magnetic field of 30 μ T. The peak temperature was held for 15 min for the first heating (TRM1) and 30 min for the second heating (TRM2) and then cooled to room temperature over 1 h. The ARM was acquired by superimposing a 180 mT peak AF on a 50 μ T DC bias magnetic field before and after the heating step. The ARMs before and after the first heating and ARM after the second heating are referred to as ARM0, ARM1, and ARM2, respectively. The ARM correction was performed using the following equations:

$$\text{TRM1}^* = \text{TRM1} \times \text{ARM0}/\text{ARM1}$$

$$\text{TRM2}^* = \text{TRM2} \times \text{ARM1}/\text{ARM2}$$

We adopted the following acceptance criteria, the same as those used in recent API studies using the Tsunakawa–Shaw method (e.g., Yamamoto et al. 2022).

1. Primary components are separated from the NRM by the stepwise AF demagnetization. The maximum angular deviation (Kirschvink 1980) is smaller than 10°.
2. One segment within the coercivity range of the primary NRM component that provides a linear relationship in the NRM-TRM1* diagram. This segment spans at least 30% of the initial NRM ($f_N \geq 0.30$). The correlation coefficient of the segments is not smaller than 0.995 ($r_N \geq 0.995$).
3. One segment also gives a linear relationship on the TRM1-TRM2* diagram. This segment spans at least 30% of the initial TRM1 ($f_T \geq 0.30$). The correlation coefficient of the segments is not smaller than 0.995 ($r_T \geq 0.995$). The slope of the segment coincides with the line with a slope of 1 within the experimental error ($1.05 \geq \text{slope}_T \geq 0.95$), proving that the ARM correction is valid. The highest coercivity of the segment is fixed to be the same as that of the NRM-TRM1* diagram.

Results

Grain densities, magnetic susceptibility, and NRM measurements

The grain density, magnetic susceptibility, and initial NRM intensity were summarized in Table 1. The grain densities of the specimens from all sites show 2.93–2.99

Table 1 Rock magnetism properties, density, and paleointensity results of lava samples collected by YK05-16 6K#926

Specimen ID	Rock type	Density (g/cm ³)	NRM meas. (10 ³ Am ²)	NRM (A/m)	χ(SI)	M _s (Am ²)	M _s (μAm ²)	H _c (mT)	H _{cr} (mT)	B _c /B _c	M _s /M _s	lower T _c (°C)	NRM			Second heating						F _{pas} (μT)	F _{pas} (μT)	S.D. S.D. (%)									
													H _L	H _H	H _M	MDF	H _L	H _H	H _M	f _N	f _H				f _M	slope _N	slope _H	slope _M	f _r	f _r			
6K#926R01-02-1	Basalt	2.99	8.045E-02	19.84	0.0066	1.790	3.145	22.81	17.94	1.2715	0.5692	213	0	180	0.56	17	0	180	0.892	1.543	1.000	1.000	0	180	1.026	<u>1.142</u>	0.999	1.000	300	rejected			
6K#926R01-02-2	Basalt		7.020E-02	19.98	0.0057	1.773	3.214	21.22	16.46	1.2892	0.5516	208	0	180	0.53	19	0	180	0.938	1.424	0.999	1.000	0	180	1.005	<u>1.185</u>	1.000	1.000	300	rejected			
6K#926R01-02-3	Basalt		6.979E-02	18.88	0.0049																												
6K#926R01-02-4	Basalt		6.638E-02	18.76	0.0045																												
6K#926R02-02-1	Basalt	2.98	6.477E-02	18.83	0.0054	3.791	6.207	26.10	21.45	1.2168	0.6108	214	2	180	0.62	23	2	180	0.890	1.468	1.000	0.991	2	180	0.998	<u>1.175</u>	1.000	0.989	300	rejected			
6K#926R02-02-2	Basalt		5.398E-02	18.49	0.0020	2.427	3.682	31.51	25.96	1.2138	0.6592	193	4	180	0.58	27	4	180	0.896	1.242	1.000	0.991	4	180	0.997	<u>1.176</u>	1.000	0.990	300	rejected			
6K#926R02-02-4	Basalt		6.463E-02	19.68	0.0049																												
6K#926R02-02-5	Basalt		4.040E-02	17.47	0.0047																												
6K#926R03-01-1	Basalt	2.96	7.277E-03	1.73	0.0008																												
6K#926R03-01-2	Basalt		3.160E-02	7.07	0.0017																												
6K#926R03-01-3 ^a	Basalt		5.016E-02	13.43	0.0029	1.692	2.445	39.99	33.61	1.1898	0.6920	226	16	180	0.74	32	16	180	0.869	1.023	1.000	0.903	16	180	0.992	<u>1.106</u>	1.000	0.904	300	rejected			
6K#926R03-01-4	Basalt		6.502E-02	17.04	0.0052	1.730	2.616	34.26	27.76	1.2341	0.6613	207	12	180	0.62	23	12	180	0.857	1.200	1.000	0.887	12	180	1.010	<u>1.186</u>	1.000	0.991	300	rejected			
6K#926R04-01-3	Basalt	2.95	5.175E-02	20.86	0.0051																												
6K#926R04-01-5	Basalt		4.939E-02	19.57	0.0051																												
6K#926R04-01-6	Basalt		6.975E-02	23.22	0.0057	1.061	1.751	20.41	16.50	1.2370	0.6059	172	12	180	0.62	19	12	180	0.871	1.329	0.999	0.802	12	180	0.994	<u>1.182</u>	0.999	0.734	300	rejected			
6K#926R05-01-1	Basalt	2.97	5.662E-02	19.02	0.0051																												
6K#926R05-01-2	Basalt		6.042E-02	18.91	0.0056	2.849	4.759	23.97	19.49	1.2299	0.6273	174	10	180	0.56	23	10	180	0.897	1.369	1.000	0.959	0	180	1.020	<u>1.157</u>	0.999	1.000	300	rejected			
6K#926R05-01-3	Basalt		4.890E-02	15.71	0.0042																												
6K#926R05-01-4	Basalt		5.755E-02	17.11	0.0049																												
6K#926R06-02-1	Basalt	2.95	4.515E-02	16.21	0.0046	1.362	2.003	29.75	24.53	1.2128	0.6800	202	4	180	0.62	23	4	180	0.958	1.198	1.000	0.988	0	180	1.012	<u>1.143</u>	1.000	1.000	300	rejected			
6K#926R06-02-2	Basalt		4.515E-02	17.22	0.0044	1.247	1.915	29.74	24.50	1.2139	0.6512	193	4	180	0.57	25	4	180	0.955	1.199	1.000	0.989	4	180	1.023	<u>1.162</u>	1.000	0.981	300	rejected			
6K#926R06-02-3	Basalt		3.768E-02	14.75	0.0044																												
6K#926R06-02-4	Basalt		3.768E-02	15.44	0.0043																												
6K#926R07-01-1	Basalt	2.93	2.624E-02	8.07	0.0017	0.611	0.807	96.82	81.30	1.1909	0.7571	264	0	180	0.56	57	0	180	0.846	1.085	1.000	1.000	0	180	1.024	0.978	0.999	1.000	300	32.6	33.0	1.0	3.0
6K#926R07-01-3	Basalt		2.824E-02	8.76	0.0019	0.809	1.133	45.85	38.80	1.1817	0.7137	233	8	180	0.48	52	8	180	0.859	1.138	0.999	0.988	8	180	0.997	1.028	1.000	0.991	300	34.1			
6K#926R07-01-4	Basalt		1.796E-02	5.23	0.0012																												
6K#926R07-01-5	Basalt		1.144E-02	3.15	0.0010																												
6K#926R08-01-1	Basalt	2.95	6.383E-03	2.40	0.0008	0.509	0.701	99.34	76.61	1.2967	0.7257	331	0	180	0.53	67	0	180	0.925	1.239	0.999	1.000	0	180	0.995	1.000	0.999	1.000	300	37.2	35.8	1.7	4.7
6K#926R08-01-2	Basalt		1.214E-02	5.22	0.0011	0.532	0.715	98.61	77.89	1.2660	0.7440	295	0	180	0.61	77	0	120	0.822	1.130	1.000	0.845	0	120	1.012	0.951	1.000	0.868	300	33.9			
6K#926R08-01-3	Basalt		2.032E-02	8.51	0.0017																												
6K#926R08-01-4	Basalt		3.096E-02	11.09	0.0020																												

Column headings: NRM meas., intensity for NRM before low-temperature demagnetization; χ, magnetic susceptibility; B_c/B_c, the ratio of coercivity of remanence to coercivity; M_s/M_s, the ratio of saturation remanence to saturation magnetization; lower T_c, lower curie temperature; H_L, H_H, low and high limit of the interval of AF steps chosen for the determination of a characteristic direction or a linear segment; MAD, maximum angular deviation of a primary component in NRM; MDF, median destructive field for NRM; slope_N, slope_H, slope_M, slope values determined from all data points after LTD in each of the ARM0-ARM1 and ARM1-ARM2 diagrams; slope_N, slope, slopes of the linear segments in the NRM-TRM1* and TRM1-TRM2* diagrams; f_N, f_H, f_M, correlation coefficients of the linear NRM-TRM1* and TRM1-TRM2* segments; f_N, f_H, f_M and TRM1 fractions of the linear NRM-TRM1* and TRM1-TRM2* segments; F_{pas}, laboratory DC field during the TRM1 and TRM2 acquisitions; F_{pas}, calculated paleointensity; F_{pas}, mean paleointensity for each site; S.D. (μT): 1σ standard deviation to F_{pas} S.D. (%): the ratio of 1σ standard deviation to F_{pas}; Arabic numbers with underline numbers denote the values failing to meet the corresponding acceptance criterion

^a Only a small amount of glass is present on the surface of 6K#926R03-01-3

(g/cm³), which are typical values for basalts. The magnetic susceptibility and initial NRM intensities range 0.0008–0.0066 (SI) and 1.73–23.22 (A/m), respectively.

Rock magnetism

Four representative results of the thermomagnetic analysis are shown out of the 16 results (Fig. 2a–d) (see Additional file 1: Fig. S3 for the other results). The 16 chip

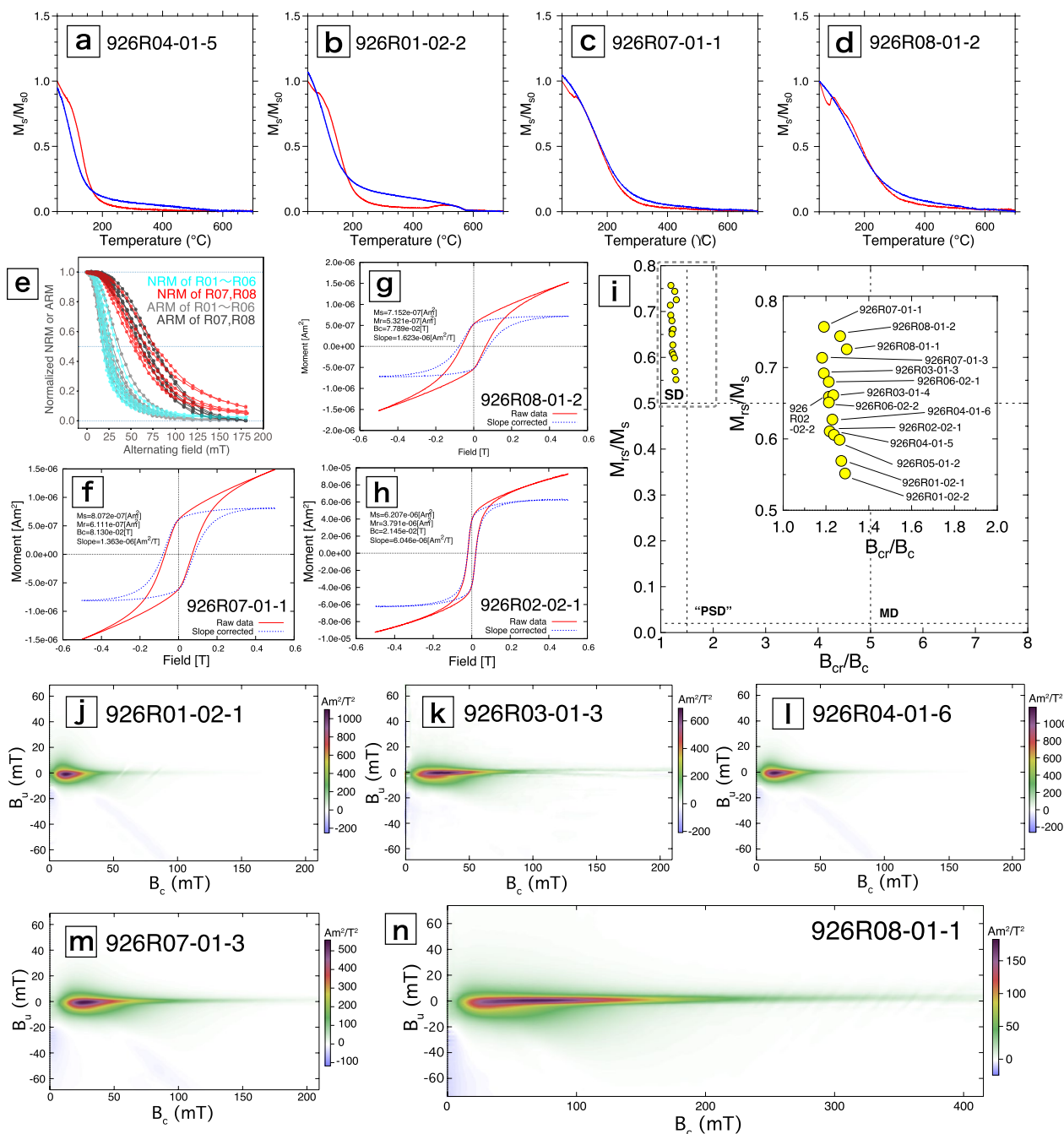


Fig. 2 Results of rock magnetic measurements. **a–d** Typical thermomagnetic curves heated in vacuum (Red line: heating procedure, blue line: cooling procedure). **e** AF demagnetization curves of NRM and ARM. **f–h** Typical hysteresis loops before (red) and after (blue) paramagnetic correction. The paramagnetic correction was performed based on the assumption that the titanomagnetite is saturated at 0.5 T. **i** Relation between the hysteresis ratios of the ratio of coercivity of remanence to coercivity (B_{cr}/B_c) and the ratio of saturation remanence to saturation magnetization (M_{rs}/M_s) for the chip samples. **j–n** FORC diagrams of representative specimens, each of which is drawn from 169 FORCs with the maximum applied magnetic field was 1.0 T

samples show major curie temperature (T_{cs}) between 170 and 340 °C, with another minor T_{cs} between 450 and 600 °C. Fifteen chip samples exhibited the intersections in the heating and cooling curves (Fig. 2a, b, and d). Only one chip sample from site R07 exhibited a completely reversible thermomagnetic curve (Fig. 2c). Three chip samples from sites R01 through R03 showed very slight signs of bumping in areas higher than 450 °C, common in low-temperature oxidized samples (Fig. 2b). The differences between the curves before and after the intersection varied from sample to sample. The initial NRM intensities up to 20 A/m is consistent with the magnetic-anomaly-derived absolute magnetization in these regions (Fujii et al. 2016; Fujii and Okino 2018). The magnetic susceptibility results have a positive correlation with the initial NRM intensities (Additional file 1: Fig. S4). The relationship implies that samples with larger amount of ferromagnetic minerals, which might be produced in slower magma cooling, carry stronger values of NRM. Furthermore, the slope of the NRM-susceptibility diagram shows sharper in lower susceptibility values, probably indicating that magnetization acquisition is efficient in the early stage of crystallization.

The results of the NRM stepwise AF demagnetization can be divided into two groups (Fig. 2e). The first is the magnetically hard group, with median destructive fields (MDFs) ranging from 52 to 77 mT (red in Fig. 2e). The second is a magnetically soft group with MDFs ranging from 17 to 32 mT (blue in Fig. 2e). The similar character is observed in the demagnetization curves of ARM (Fig. 2e).

Typical magnetic hysteresis loops are shown in Fig. 2f–h. There are two types of loops: wide (Fig. 2f, g) and narrow (Fig. 2h). Figure 2i shows a biplot of the hysteresis parameters for the 15 chip samples from eight sites. All data points are distributed in the single domain (SD) region based on the day plot (e.g., Day et al. 1977), with the ratio of saturation remanence to saturation magnetization (M_{rs}/M_s) exceeding 0.5. The M_{rs}/M_s for all the samples exceeded 0.5, the theoretical upper limit for a randomly oriented uniaxial grain ensemble. This is a common observation in MORBs (e.g., Gee and Kent 1995; Carlot and Kent 2002). These

results are either due to an overestimated value when the M_s value is not fully saturated (Fabian 2006) or to the presence of multiaxial SD grains (Mitra et al. 2011). See Additional file 1: Fig. S5 for all the hysteresis loops.

The FORC diagrams of 6K#926R01, 6K#926R03, 6K#926R04, 6K#926R07, and 6K#926R08 show closed teardrop contours with some magnetostatic interactions (B_u within $\pm \sim 20$ mT) and the negative region along the negative part of B_u axis, which means that the chip samples mainly include SD grains (Fig. 2j–n). The FORC diagrams of 6K#926R03 and 6K#926R08 indicate elongated coercivity distributions at $B_u=0$. In particular, the FORC diagram of 6K#926R08 indicates a sharp ridge along the B_c axis (>400 mT), similar to central ridges observed in the marine sediments (e.g., Egli et al. 2010).

Paleointensity measurement

The results of the API experiments for a total of 18 specimens, two or three from each of the eight sites, are summarized in Table 1. All NRM directions show a single component toward the origin of the orthogonal projection (Fig. 3; Table 1), and all maximum angular deviations of the NRM are less than 0.8. The representative results of the Tsunakawa–Shaw method are shown in Fig. 3a, b. Six specimens from two sites (6K#926R07 and 6K#926R08) passed the acceptance criteria of the Tsunakawa–Shaw method. The specimen-level APIs are 32.3 to 34.1 μ T for 6K#926R07 (site-level mean is 33.0 ± 1.0 μ T [$N=3$, 1σ]), 33.9 to 37.2 μ T for 6K#926R08 (site-level mean is 35.8 ± 1.7 μ T [$N=3$, 1σ]). The standard deviations are 3.0% and 4.7% of the mean, respectively, indicating highly precise APIs. See Additional file 1: Fig. S6 for the other accepted results. This is the first API measurement ever obtained from MORB using the Tsunakawa–Shaw method. The remaining 12 specimens are rejected by the acceptance criteria. All of them are rejected because the slope of the TRM1*–TRM2 diagram (slope $_{\tau}$) exceeded the range of 1.00 ± 0.05 (Table 1; Fig. 3). See Additional file 1: Fig. S7 for the other rejected results. The acceptance rate for the API measurements in this study is 33.3%. The amount of change in ARM between before and after the LTD treatment was of -3.6 to 2.9%.

(See figure on next page.)

Fig. 3 Typical examples of accepted and rejected results of the Tsunakawa–Shaw paleointensity experiments: **(a)** an accepted result with little change in ARM after either the first or the second heating steps, **(b)** a rejected result with the slope of a linear segment on the TRM1–TRM2* diagram (slope $_{\tau}$) is out of 1.00 ± 0.05 . FRAC in NRM–TRM1* (TRM1–TRM2*) diagram is f_N (f_{τ}). Δ AIC is Akaike's Information Criterion. k is curvature value of linear segment in each diagram defined by Paterson (2011) (k' is defined by Paterson et al. 2014). **(c)** Slopes of a linear segment on the NRM–TRM1* diagram (slope $_{N}$) for each specimen. **(d)** Slope $_{\tau}$ for each specimen. Black dashed line and gray area shows the acceptance range of 1.00 ± 0.05 . **(e)** Comparison of paleointensity values obtained from the two sites. Red (black) circle is specimen-level (site-level mean) paleointensities. Black error bars are standard deviations (1σ). The dotted black line indicates the present geomagnetic intensity around the diving sites according to the IGRF-13 model. Light blue (light green) area is the standard deviation range of site 6K#926R07 (6K#926R08)

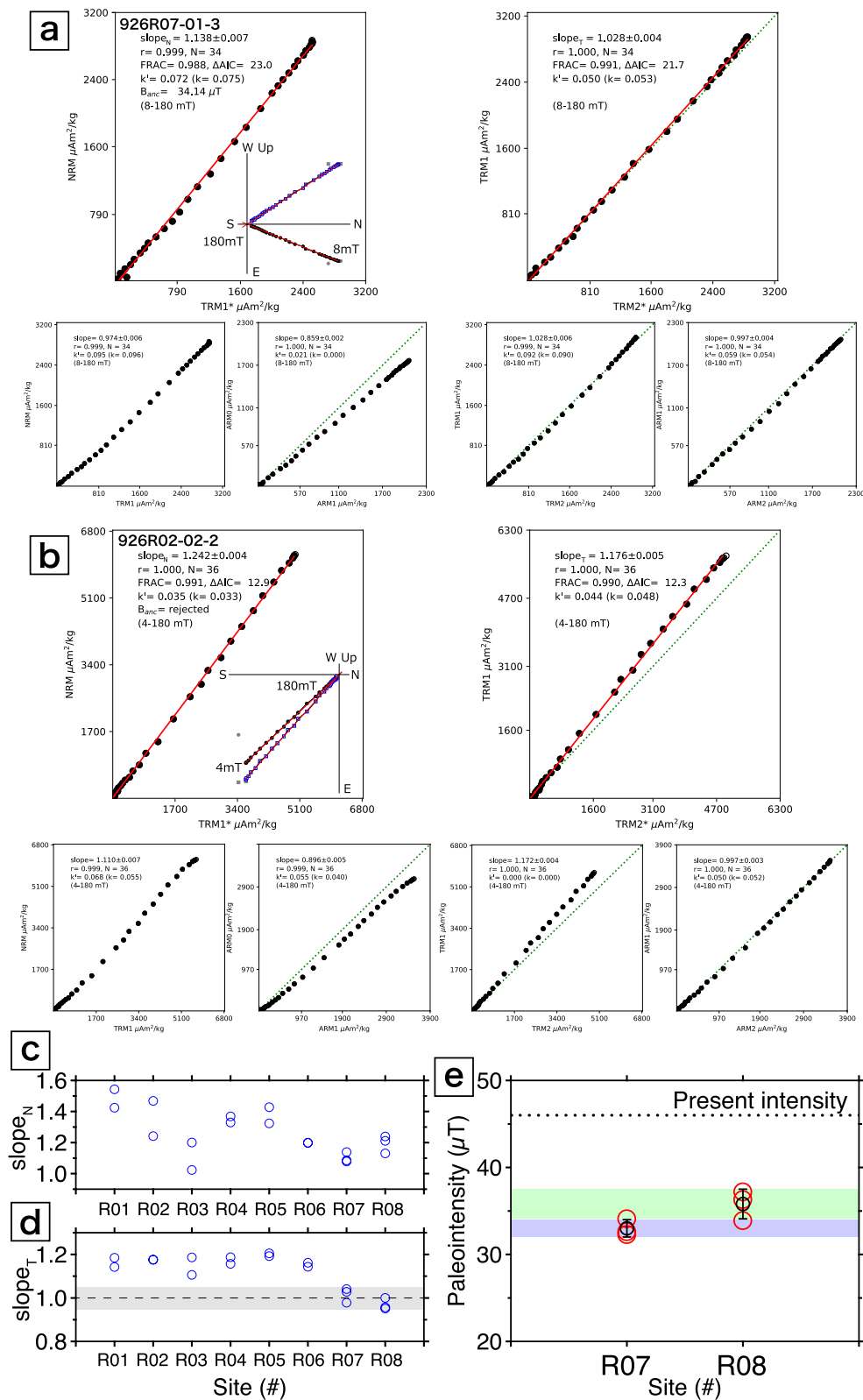


Fig. 3 (See legend on previous page.)

Discussion

Characteristics of paleointensity results and the cause of acceptance/rejection

In this subsection, we discuss the characteristics of the parameters of the API results and the causes of acceptance or rejection. The standard deviations of the site-level API means are small (<5%). This is probably because the MORBs did not acquire TCRM, unlike subaerial basalts, thereby preventing the mixture situation of accurate and overestimated API results. Based on the results of FORC and thermomagnetic analyses, we can estimate that the analyzed MORBs are dominated by titanium-rich SD grains with no MD grains. There was no significant difference between ARM0 and ARM1 (slope_{AI} ranged from 0.822 to 0.958), indicating little thermal alteration by heating. This suggests that on-axis submarine basalts were suitable for API experiments. We interpreted these factors as successful API measurement using the Tsunakawa-Shaw method. The Coe-Thellier method (Coe 1967) may also be applicable to API measurements for MORBs in future studies.

The variation in the slope_N values from specimens from sites 6K#926R01 to 6K#926R06 (1.023–1.543) was larger than those of specimens from sites 6K#926R07 and 6K#926R08 (1.078–1.239; Fig. 3c; Table 1). The slope_T of specimens from sites 6K#926R01 to 6K#926R06 (1.106–1.205) was clearly different from those of specimens from sites 6K#926R07 and 6K#926R08 (0.951–1.041; Fig. 3d; Table 1). The trend of slope_T suggests that the mechanism by which MORBs are rejected in the API experiments may be common. The mechanism is likely unusual alteration process; the coercivity spectrum of TRM decreased after the second heating, even though the ARM coercivity spectrum did not change.

Rock-magnetic difference between accepted and rejected paleointensity results

The shared characteristics of the specimens that passed the API acceptance criteria, compared to the samples that did not, were (1) high T_c (Fig. 2c, d; Table 1), (2) low initial NRM intensity (Table 1), (3) high MDF of NRM and ARM (Fig. 2e; Table 1), and (4) high M_{rs}/M_s (>0.7; Fig. 2i) and wide hysteresis loops (Fig. 2f, g). The accepted specimens from sites 6K#926R07 and 6K#926R08 show relatively high T_c s of 233 °C to 331 °C, whereas the rejected specimens from the other sites show relatively low T_c s of 172 °C to 226 °C. These results indicate that the remanence carriers in the accepted and rejected specimens were relatively low- and high-Ti titanomagnetite, respectively. The previously reported geochemical composition of TiO₂/FeO is consistent across the sites (Sato et al. 2015; Neo 2011) (Additional file 2: Table S1; Additional file 1: Fig. S8), independent of the trend of T_c s. We found

no systematic differences in the FORC diagrams between the accepted and rejected specimens. All accepted specimens contained hard magnetic minerals, as indicated by the high MDF of NRM and ARM. The specimens from sites 6K#926R07 and 6K#926R08 indicate M_{rs}/M_s values greater than 0.7, whereas all the rejected specimens had M_{rs}/M_s values less than 0.7. These results suggest that high T_c , low initial NRM intensity, high MDF of the NRM, and high M_{rs}/M_s could be useful for the pre-selection of MORB specimens for API experiments.

On the other hand, an exceptional feature of more elongated ridge along the B_c axis (>400 mT) with a higher coercivity peak (~70 mT) in FORC diagram was found in the chip sample from site 6K#926R08 (Fig. 2n). This may be associated with the sheeted morphology of the site. Considering the feature of the FORC diagram with high MDF and T_c of the 6K#926R08 chip sample, it suggests the possible presence of elongated or needle-shaped low Ti titanomagnetite grains in the chip sample.

Paleointensity dating

The two site-level API means (33.0 ± 1.0 and 35.8 ± 1.7 μ T) are very close to each other (Fig. 3e). Because the two lavas with different morphologies (6K#926R07: pillow lava, 6K#926R08: sheet lava) showed similar APIs, they may have erupted almost simultaneously. This is consistent with the geological observations and petrological descriptions. However, they are slightly distinguishable at one standard deviation (1σ) level. Based on the rate of change in geomagnetic intensity (0.015–0.067 μ T/year) estimated from the IGRF-13 (Alken et al. 2021) and gufm1 (Jackson et al. 2000) models from 1590 to 2023 CE, there may be a time difference of $(35.8 - 33.0 \mu\text{T}) / 0.015$ or 0.067 ($\mu\text{T}/\text{year}$) = 42–187 years between the two lavas.

The site-level API means are approximately 0.7–0.8 times the present geomagnetic intensity of 46.07 μ T calculated using IGRF-13 (Alken et al. 2021) at the study site (latitude $-24^\circ 53'$; longitude $69^\circ 58'$). Additionally, considering their standard deviations (1σ), the API means can be distinguished from the present geomagnetic intensity. This means that these lavas erupted at somewhat earlier time than the present. To estimate the upper limit of the eruption timing of the studied lavas, we compared the site-level APIs with the model made up of the IGRF-13 model with the gufm1 model (Jackson et al. 2000), which allows high-precision reconstruction of the API variation from the present back to 1590 CE (Fig. 4). The geomagnetic intensity from 1590 to 2023 CE always exceeds 40 μ T (Fig. 4; Additional file 3: Table S2). The minimum intensity in 1590 CE was 40.43 μ T. This value does not overlap with the range of standard deviations of our site-level API means. Therefore, it is constrained that the conical cone erupted before 1590 CE. In addition, the conical

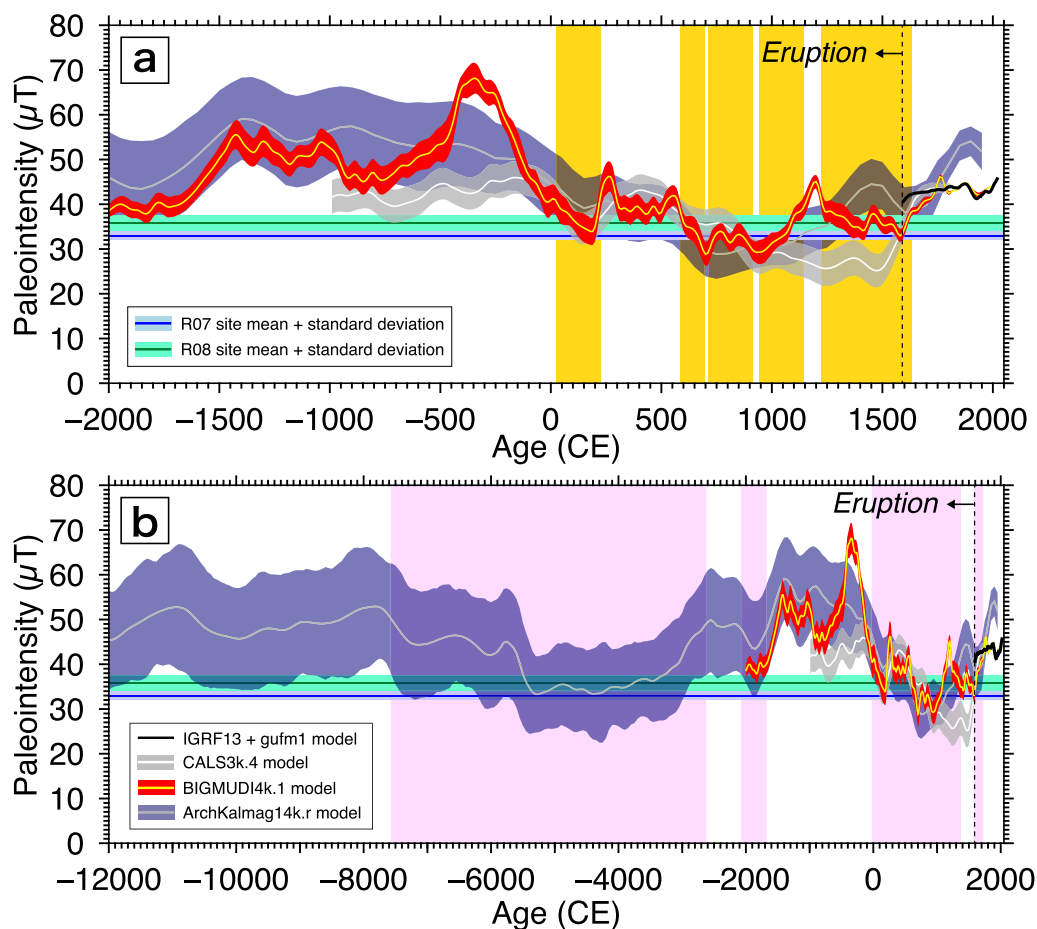


Fig. 4 Comparison of our two site-level API means (blue and green lines) with the geomagnetic intensity curves over (a) 4 ka and (b) 14 ka calculated from the IGRF-13 (Alken et al. 2021) + gufm1 (Jackson et al. 2000) (black curve), CALS3k.4 (Korte and Constable 2011) (white line), BIGMUDI4k.1 (Arneitz et al. 2019) (yellow line), and ArchKalmag14 k.r (Schanner et al. 2022) (gray line) geomagnetic models. Colored areas along geomagnetic intensity curves indicate the standard deviation range. The black dashed vertical line indicates the upper limit of eruption timing of the conical cone on the CIR-S2 constrained by the IGRF-13 + gufm1 model. The Orange (light purple) areas indicate overlapping time interval between the two site-level API means and the BIGMUDI4k.1 (ArchKalmag14k.r) geomagnetic intensity curve

cone erupted after ~ 0.77 Ma because the sampling sites locate between the both Brunhes-Matuyama boundary identified in the sea-surface magnetic anomalies (Fig. 1) (Okino et al. 2015). We can robustly estimate that the conical cone erupted before 1590 CE and after ~ 0.77 Ma.

Next, we further consider to improve the age constraint by comparing with the CALS3k.4 (Korte and Constable 2011) (Additional file 4: Table S3), BIGMUDI4k.1 (Arneitz et al. 2019) (Additional file 5: Table S4), and ArchKalmag14k.r (Schanner et al. 2022) (Additional file 6: Table S5) models (Fig. 4). The latest two models include new archeointensity data from African continent (e.g., Tarduno et al. 2015; Osete et al. 2015; Casas et al. 2016), which is relatively close to the CIR. They also include only data from archeologic and volcanic materials, avoiding the smoothing effect of sediment data. Therefore, we consider that the two latest geomagnetic

models are more suitable than the CALS3k.4 model for dating the conical cone using our API data.

Over the last 4000 years, which is the temporal limitation of the BIGMUDI4k.1 model, we find five overlapping age intervals between the both of two site-level API means and the BIGMUDI4k.1 paleointensity curve at the standard deviation level (orange zones in Fig. 4a). The overlap is in the time interval from -25 CE to 1635 CE. Combined with the above-mentioned robust age constraint of ~ 0.77 Ma to 1590 CE, it suggests that the conical cone may have erupted within a period of -25 to 1590 CE. Over the last 14,000 years, which is the temporal limitation of the ArchKalmag14k.r model, we find four overlapping age intervals between the both of two site-level API means and the ArchKalmag14 k.r paleointensity curve at the standard deviation level (light purple zones in Fig. 4b). Combined with the primary robust

constraint of ~0.77 Ma to 1590 CE, the conical cone may have erupted within a period of –7575 CE to –2625 CE, –2075 CE to –1675 CE, –25 CE to 1375 CE, or 1575 CE to 1590 CE (–7575 CE to –1675 CE or –25 CE to 1590 CE, roughly divided). By the comparisons with the BIGMUDI4k.1 and ArchKalmag14 k.r models, we can further constrain the overlap in the periods of –25 to 1375 CE and 1575 to 1590 CE. If these constraints are plausible, volcanism on the slow- to intermediate-rate spreading ridge may have occurred relatively frequently on a millennial-scale and possibly impacted abyssal environment. To further constrain the eruption age, not only the API but also the paleomagnetic declination and inclination are required. We should sample orientated submarine basalts in future studies.

Conclusions

The Tsunakawa–Shaw method was first applied to MORBs collected from the volcanic conical cone in the NVZ of CIR-S2, providing the six APIs of 32.3–37.2 μT from six specimens (three specimens each from two lava sites, 6K#926R07 and 6K#926R08). Although the FORC diagram results did not differ significantly among the chip samples, specimens with high T_c , low initial NRM intensity, high MDFs of NRM and ARM, and large values of the hysteresis ratios of M_{rs}/M_s tended to be accepted in the API experiments. Using this trend, we should be able to increase the success rate of API measurements from MORBs. Although the lavas at the two sites had different morphologies (pillow vs. sheet lava), their site-level API means were similar. Therefore, these lavas are suggested to erupt within a short period. The primary comparison between our two API site means and the 1590–present high-resolution IGRF-13+gufm1 model constrains the eruption timing of the studied conical cone to be <1590 CE. Considering the overlapping between the two site-level API means and paleointensity curves calculated from the BIGMUDI4k.1 and ArchKalmag14k.r models, we can estimate that the conical cone may have erupted in –7575 CE to –1675 CE or –25 CE to 1590 CE. Although we could not determine the unique eruption timing of the NVZ conical cone of CIR-S2, we demonstrated that the measuring APIs provides a helpful information for investigating the history of volcanic eruptions and lava emplacements in the abyssal environment.

Abbreviations

AF	Alternating field
AORI	Atmosphere and Ocean Research Institute
API	Absolute paleointensity
ARM	Anhysteretic remanent magnetization
CIR	Central Indian Ridge
FORC	First-order reversal curve
JAMSTEC	Japan Agency for Marine-Earth Science and Technology

MORB	Mid-ocean ridge basalt
MD	Multi domain
MDF	Median destructive field
NRM	Natural remanent magnetization
NTD	Non-transform discontinuity
SD	Single domain
TRM	Thermal remanent magnetization

Supplementary Information

The online version contains supplementary material available at <https://doi.org/10.1186/s40623-024-01963-3>.

Additional file 1: Figure S1. (a–h) Photographs of samples of studied volcanic rocks collected from the neo-volcanic zone of CIR-S2. **Figure S2.** How to prepare the specimens and the chip samples. **Figure S3.** All results of thermomagnetic curves heated in vacuum (Red line: heating procedure, blue line: cooling procedure). The top panel shows the rejected samples in the Tsunakawa-Shaw method and the bottom panel shows the accepted samples. **Figure S4.** The relationship between magnetic susceptibility and initial NRM intensity. **Figure S5.** All Hysteresis loops before (red) and after (blue) paramagnetic correction, respectively. The top panel shows the rejected samples in the Tsunakawa-Shaw method and the bottom panel shows the accepted samples. **Figure S6.** (a–e) The other accepted results of the Tsunakawa-Shaw paleointensity experiments. **Figure S7.** (a–k) The other rejected results of the Tsunakawa-Shaw paleointensity experiments. **Figure S8.** Variations of TiO_2 and FeO^* contents of Sato et al. (2015) and Neo (2011) with site number of the conical cone in the CIR-S2. *Total Fe as FeO .

Additional file 2: Table S1. Major and trace element data of previous studies.

Additional file 3: Table S2. Geomagnetic intensity data from 1590 to 2023 at the diving site calculated by NCEI Geomagnetic Calculator.

Additional file 4: Table S3. Paleointensity predictions of CALS3K.4 calculated by GEOMAGIA v3.

Additional file 5: Table S4. Paleointensity predictions of BIGMUD4k.1 calculated by Conrad Observatory Data Portal.

Additional file 6: Table S5. Paleointensity predictions of ArchKalmag14k.r calculated by Kalmag.

Acknowledgements

We are grateful to the onboard scientific parties and crews of the R/V Yokusuka YK05-16 Leg.1 cruise, and the support team of the submersible *SHINKAI 6500*. We thank Takayuki Tomiyama and Hiromichi Soejima for sampling at JAMSTEC. We thank Yusuke Yokoyama, Yosuke Miyairi, Toshitsugu Yamazaki, and Yuhji Yamamoto for using the measurement instruments at their laboratories. We thank Hiroshi Sato, Hidenori Kumagai, and Kentaro Nakamura for providing the geochemical data. We thank Kyoko Okino for providing the compiled bathymetry data. We thank Masao Ohno, Chie Kato, Kohei Masaoka, Naoto Ishikawa, Yuhji Yamamoto, Nobutatsu Mochizuki, Koji Fukuma, Hidetoshi Shibuya, Yoichi Usui, Hirokuni Oda, Akira Ishikawa, and Takeshi Matsumoto for their helpful comments. Rock samples archived in DARWIN database, managed by JAMSTEC, were used in this study. The part of this study was conducted under the cooperative research program of Marine Core Research Institute (MaCRI), Kochi University. The magnetic hysteresis loops were drawn using MagePlot (Hatakeyama 2018) (<http://mage-p.org/mageplot/>). Constructive reviews by two anonymous reviewers and guest editor Hyeon-Seon Ahn greatly improved the manuscript.

Author contributions

YY and MF prepared the samples and wrote the manuscript. YY conducted all experiments. MF helped a part of experiments. All authors read and approved the final manuscript.

Funding

This study was supported by Grant-in-Aid (Early-Career Scientists) (No. JP22K14124), and Grant-in-Aid (B) (No. JP22H01337).

Availability of data and materials

The datasets used and/or analyzed in this study are available from the corresponding author upon reasonable request.

Declarations**Ethics approval and consent to participate**

Not applicable.

Consent for publication

Not applicable.

Competing interests

Not applicable.

Author details

¹Division of Environmental Changes, Faculty of Social and Cultural Studies, Kyushu University, 744 Motoooka, Fukuoka 819-0395, Japan. ²National Institute of Polar Research, 10-3 Midori-Cho, Tachikawa, Tokyo 190-8518, Japan. ³The Graduate University for Advanced Studies, SOKENDAI, 10-3 Midori-Cho, Tachikawa, Tokyo 190-8518, Japan.

Received: 31 August 2023 Accepted: 7 January 2024

Published online: 30 January 2024

References

- Ahn H, Yamamoto Y (2019) Paleomagnetic study of basaltic rocks from Baengnyeong Island, Korea: efficiency of the Tsunakawa-Shaw paleointensity determination on non-SD-bearing materials and implication for the early Pliocene geomagnetic field intensity. *Earth Planets Space* 71(1):1–20. <https://doi.org/10.1186/s40623-019-1107-6>
- Alken P, Thébaud E, Beggan CD, Amit H, Aubert J, Baerenzung J, Zhou B (2021) International geomagnetic reference field: the thirteenth generation. *Earth Planets Space* 73(1):1–25. <https://doi.org/10.1186/s40623-020-01288-x>
- Arneitz P, Egli R, Leonhardt R, Fabian K (2019) A Bayesian iterative geomagnetic model with universal data input: Self-consistent spherical harmonic evolution for the geomagnetic field over the last 4000 years. *Phys Earth Planet Inter* 290:57–75
- Biasi J, Kirschvink JL, Fu RR (2021) Characterizing the geomagnetic field at high southern latitudes: evidence from the antarctic peninsula. *J Geophys Res Solid Earth* 126(12):e2021JB023273
- Bowles J, Gee JS, Kent DV, Perfit MR, Soule SA, Fornari DJ (2006) Paleointensity applications to timing and extent of eruptive activity, 9–10 N East Pacific Rise. *Geochem Geophys Geosyst.* <https://doi.org/10.1029/2005GC001141>
- Briais A (1995) Structural analysis of the segmentation of the Central Indian Ridge between 20°30′ S and 25°30′ S (Rodriguez Triple Junction). *Mar Geophys Res* 17(5):431–467
- Carlut J, Kent DV (2000) Paleointensity record in zero-age submarine basalt glasses: testing a new dating technique for recent MORBs. *Earth Planet Sci Lett* 183(3–4):389–401
- Carlut J, Kent DV (2002) Grain-size-dependent paleointensity results from very recent mid-oceanic ridge basalts. *J Geophys Res Solid Earth* 107(B3):EPM-2
- Carlut J, Cormier MH, Kent DV, Donnelly KE, Langmuir CH (2004) Timing of volcanism along the northern East Pacific Rise based on paleointensity experiments on basaltic glasses. *J Geophys Res Solid Earth.* <https://doi.org/10.1029/2003JB002672>
- Casas L, Fouzai B, Prevosti M, Laridhi-Ouazaa N, Jarrega R, Baklouti S (2016) New archaeomagnetic data from Tunisia: Dating of two kilns and new archaeointensities from three ceramic artifacts. *Geoarchaeology* 31(6):564–576
- Coe RS (1967) Paleo-intensities of the Earth's magnetic field determined from Tertiary and Quaternary rocks. *J Geophys Res* 72(12):3247–3262
- Day R, Fuller M, Schmidt VA (1977) Hysteresis properties of titanomagnetites: grain-size and compositional dependence. *Phys Earth Planet Inter* 13(4):260–267
- DeMets C, Gordon RG, Argus DF (2010) Geologically current plate motions. *Geophys J Int* 181(1):1–80
- Dunlop DJ, Hale CJ (1976) A determination of paleomagnetic field intensity using submarine basalts drilled near the Mid-Atlantic Ridge. *J Geophys Res* 81(23):4166–4172
- Egli R (2013) VARIFORC: an optimized protocol for calculating non-regular first-order reversal curve (FORC) diagrams. *Global Planet Change* 110:302–320
- Egli R, Chen AP, Winklhofer M, Kodama KP, Hornig CS (2010) Detection of noninteracting single domain particles using first-order reversal curve diagrams. *Geochem Geophys Geosyst.* <https://doi.org/10.1029/2009GC002916>
- Fabian K (2006) Approach to saturation analysis of hysteresis measurements in rock magnetism and evidence for stress dominated magnetic anisotropy in young mid-ocean ridge basalt. *Phys Earth Planet Inter* 154(3–4):299–307
- Fujii M, Okino K (2018) Near-seafloor magnetic mapping of off-axis lava flows near the Kairei and Yokoniwa hydrothermal vent fields in the Central Indian Ridge. *Earth Planets Space* 70(1):1–17. <https://doi.org/10.1186/s40623-018-0959-5>
- Fujii M, Okino K, Sato T, Sato H, Nakamura K (2016) Origin of magnetic highs at ultramafic hosted hydrothermal systems: Insights from the Yokoniwa site of Central Indian Ridge. *Earth Planet Sci Lett* 441:26–37
- Gee J, Kent DV (1995) Magnetic hysteresis in young mid-ocean ridge basalts: dominant cubic anisotropy? *Geophys Res Lett* 22(5):551–554
- Gee JS, Cande SC, Hildebrand JA, Donnelly K, Parker RL (2000) Geomagnetic intensity variations over the past 780 kyr obtained from near-seafloor magnetic anomalies. *Nature* 408(6814):827–832
- Grommé S, Mankinen EA, Marshall M, Coe RS (1979) Geomagnetic paleointensities by the Thelliers' method from submarine pillow basalts: effects of seafloor weathering. *J Geophys Res Solid Earth* 84(B7):3553–3575
- Haggerty S (1991) Chapter 5. Oxide textures-A Mini-atlas. In: Lindsley D (ed) *Oxide Minerals: Petrologic and Magnetic Significance*. De Gruyter, Berlin, Boston, pp 129–220
- Harrison RJ, Feinberg JM (2008) FORCinel: An improved algorithm for calculating first-order reversal curve distributions using locally weighted regression smoothing. *Geochem Geophys Geosyst.* <https://doi.org/10.1029/2008GC001987>
- Hatakeyama T (2018) Online plotting applications for paleomagnetic and rock magnetic data. *Earth Planets Space* 70:1–8. <https://doi.org/10.1186/s40623-018-0906-5>
- Honsho C, Tamaki K, Fujimoto H (1996) Three-dimensional magnetic and gravity studies of the Rodriguez Triple Junction in the Indian Ocean. *J Geophys Res Solid Earth* 101(B7):15837–15848
- Jackson A, Jonkers AR, Walker MR (2000) Four centuries of geomagnetic secular variation from historical records. *Philosophi Transact Royal Soc London Series Math Phys Eng Sci* 358(1768):957–990
- Juarez MT, Tauxe L, Gee JS, Pick T (1998) The intensity of the Earth's magnetic field over the past 160 million years. *Nature* 394(6696):878–881
- Kato C, Sato M, Yamamoto Y, Tsunakawa H, Kirschvink JL (2018) Paleomagnetic studies on single crystals separated from the middle Cretaceous Iritono granite. *Earth Planets Space* 70(1):1–19. <https://doi.org/10.1186/s40623-018-0945-y>
- Kirschvink J (1980) The least-squares line and plane and the analysis of palaeomagnetic data. *Geophys J Int* 62(3):699–718
- Kitahara Y, Yamamoto Y, Ohno M, Kuwahara Y, Kameda S, Hatakeyama T (2018) Archeointensity estimates of a tenth-century kiln: first application of the Tsunakawa-Shaw paleointensity method to archeological relics. *Earth Planets Space* 70(1):1–16. <https://doi.org/10.1186/s40623-018-0841-5>
- Kitahara Y, Nishiyama D, Ohno M, Yamamoto Y, Kuwahara Y, Hatakeyama T (2021) Construction of new archaeointensity reference curve for East Asia from 200 CE to 1100 CE. *Phys Earth Planet Inter* 310:106596
- Korte M, Constable C (2011) Improving geomagnetic field reconstructions for 0–3 ka. *Phys Earth Planet Inter* 188(3–4):247–259
- Macdonald K, Sempere JC, Fox PJ (1984) East Pacific Rise from Siqueiros to Orozco fracture zones: along-strike continuity of axial neovolcanic zone and structure and evolution of overlapping spreading centers. *J Geophys Res Solid Earth* 89(B7):6049–6069
- Mejia V, Opdyke ND, Perfit MR (1996) Paleomagnetic field intensity recorded in submarine basaltic glass from the East Pacific Rise, the last 69 ka. *Geophys Res Lett* 23(5):475–478

- Mitra R, Tauxe L, Gee JS (2011) Detecting uniaxial single domain grains with a modified IRM technique. *Geophys J Int* 187(3):1250–1258
- Mochizuki N, Tsunakawa H, Oishi Y, Wakai S, Wakabayashi KI, Yamamoto Y (2004) Palaeointensity study of the Oshima 1986 lava in Japan: implications for the reliability of the Thellier and LTD-DHT Shaw methods. *Phys Earth Planet Inter* 146(3–4):395–416
- Mochizuki N, Fujii S, Hasegawa T, Yamamoto Y, Hatakeyama T, Yamashita D, Shibuya H (2021) A tephra-based approach to calibrating relative geomagnetic paleointensity stacks to absolute values. *Earth Planet Sci Lett* 572:117119
- Neo, N. (2011). Petrology of the basalts of the Central Indian ridge and regional variations of MORBs along the eastern part of the southwest Indian ridge (Doctoral dissertation, Niigata University).
- Okino K, Nakamura K, Sato H (2015) Tectonic background of four hydrothermal fields along the Central Indian Ridge. In: Ishibashi, Ji., Okino, K., Sunamura, M. (eds) Subseafloor biosphere linked to hydrothermal systems: TAIGA concept, 133–146. Springer, Tokyo.
- Osete ML, Catanzariti G, Chauvin A, Pavón-Carrasco FJ, Roperch P, Fernández VM (2015) First archaeomagnetic field intensity data from Ethiopia, Africa (1615±12 AD). *Phys Earth Planet Inter* 242:24–35
- Ozima M, Ozima M, Nagata T (1964) Low temperature treatment as an effective means of “magnetic cleaning” of natural remanent magnetization. *J Geomagn Geoelectr* 16(1):37–40
- Parson LM, Patriat P, Searle RC, Briais AR (1993) Segmentation of the central Indian Ridge between 12° 12' S and the Indian Ocean triple junction. *Mar Geophys Res* 15(4):265–282
- Paterson GA (2011) A simple test for the presence of multidomain behavior during paleointensity experiments. *J Geophys Res Solid Earth*. <https://doi.org/10.1029/2011JB008369>
- Paterson GA, Tauxe L, Biggin AJ, Shaar R, Jonestrack LC (2014) On improving the selection of Thellier-type paleointensity data. *Geochem Geophys Geosyst* 15(4):1180–1192
- Pérez-Rodríguez N, Morales J, Cejudo R, Guilbaud MN, Goguitchaichvili A (2022) Reassessing the paleointensities of three quaternary volcanic structures of the-Michoacán-Guanajuato volcanic field (Mexico) through a multimethodological analysis. *Phys Earth Planet Inter* 332:106927
- Petersen N, Eisenach P, Bleil U (1979) Low temperature alteration of the magnetic minerals in ocean floor basalts. *Deep Drill Resul Atlantic Ocean Ocean Crust* 2:169–209
- Pick T, Tauxe L (1993a) Holocene paleointensities: thellier experiments on submarine basaltic glass from the East Pacific Rise. *J Geophys Res Solid Earth* 98(B10):17949–17964
- Pick T, Tauxe L (1993b) Geomagnetic palaeointensities during the Cretaceous normal superchron measured using submarine basaltic glass. *Nature* 366(6452):238–242
- Prévot M, Mankinen EA, Grommé S, Lecaille A (1983) High paleointensities of the geomagnetic field from thermomagnetic studies on rift valley pillow basalts from the Mid-Atlantic Ridge. *J Geophys Res Solid Earth* 88(B3):2316–2326
- Riisager P, Riisager J, Zhao X, Coe RS (2003) Cretaceous geomagnetic paleointensities: thellier experiments on pillow lavas and submarine basaltic glass from the Ontong Java Plateau. *Geochem Geophys Geosyst*. <https://doi.org/10.1029/2003GC000611>
- Rolph TC, Shaw J (1985) A new method of palaeofield magnitude correction for thermally altered samples and its application to Lower Carboniferous lavas. *Geophys J Int* 80(3):773–781
- Sato T, Okino K, Kumagai H (2009) Magnetic structure of an oceanic core complex at the southernmost Central Indian Ridge: analysis of shipboard and deep-sea three-component magnetometer data. *Geochem Geophys Geosyst*. <https://doi.org/10.1029/2008GC002267>
- Sato H, Nakamura K, Kumagai H, Senda R, Morishita T, Tamura A, Arai S (2015) In: Ishibashi Ji, Okino K, Sunamura M (eds) Petrology and geochemistry of mid-ocean ridge basalts from the southern central Indian ridge. Sub-seafloor Biosphere Linked to Hydrothermal Systems: TAIGA Concept, 163–175. Springer, Tokyo.
- Schanner M, Korte M, Holschneider M (2022) ArchKalmag14k: a Kalman-filter based global geomagnetic model for the Holocene. *J Geophys Res Solid Earth* 127(2):e2021JB023166
- Shaw J (1974) A new method of determining the magnitude of the palaeomagnetic field: application to five historic lavas and five archaeological samples. *Geophys J Int* 39(1):133–141
- Shcherbakov VP, Gribov SK, Lhuillier F, Aphinogenova NA, Tsel'movich VA (2019) On the reliability of absolute palaeointensity determinations on basaltic rocks bearing a thermochemical remanence. *J Geophys Res Solid Earth* 124(8):7616–7632
- Smirnov AV, Kulakov EV, Foucher MS, Bristol KE (2017) Intrinsic paleointensity bias and the long-term history of the geodynamo. *Sci Adv* 3(2):e1602306
- Smith DK, Cann JR (1990) Hundreds of small volcanoes on the median valley floor of the Mid-Atlantic Ridge at 24–30 N. *Nature* 348(6297):152–155
- Tarduno JA, Watkeys MK, Huffman TN, Cottrell RD, Blackman EG, Wendt A, Scribner C, Wagner CL (2015) Antiquity of the South Atlantic Anomaly and evidence for top-down control on the geodynamo. *Nat Commun* 6(1):7865
- Tsunakawa H, Shaw J (1994) The Shaw method of palaeointensity determinations and its application to recent volcanic rocks. *Geophys J Int* 118(3):781–787
- Yamamoto Y (2006) Possible TCRM acquisition of the Kilauea 1960 lava, Hawaii: failure of the Thellier paleointensity determination inferred from equilibrium temperature of the Fe–Ti oxide. *Earth Planets Space* 58(8):1033–1044. <https://doi.org/10.1186/BF03352608>
- Yamamoto Y, Tsunakawa H, Shibuya H (2003) Palaeointensity study of the Hawaiian 1960 lava: implications for possible causes of erroneously high intensities. *Geophys J Int* 153(1):263–276
- Yamamoto Y, Tauxe L, Ahn H, Santos C (2022) Absolute paleointensity experiments on aged thermoremanent magnetization: assessment of reliability of the Tsunakawa-Shaw and other methods with implications for “fragile” curvature. *Geochem Geophys Geosyst* 23(4):e2022GC010391
- Yoshimura Y, Yamazaki T, Yamamoto Y, Ahn H, Kidane T, Otofujii Y (2020) Geomagnetic paleointensity around 30 Ma estimated from Afro-Arabian large igneous province. *Geochem Geophys Geosyst* 21(12):e2020GC009341

Publisher's Note

Springer Nature remains neutral with regard to jurisdictional claims in published maps and institutional affiliations.